

CARMA Memorandum Series #5 ¹

Compact Configuration Evaluation for CARMA

M. C. H. Wright

*Radio Astronomy laboratory, University of California, Berkeley,
CA, 94720*

September 5, 2002

ABSTRACT

In this memo, we compare the imaging performance of three compact configurations for the CARMA telescope. We discuss ring and spiral configurations. MIRIAD scripts simulate imaging with heterogeneous arrays, and pipeline the results into tables. We present tables of beam FWHM, brightness sensitivity and sidelobe levels for source declinations from +60 to -40 degrees. Mosaic images for source diameters 32", and 40" are analyzed. The residual imaging errors are characterized by the recovered flux, peak flux density and the sidelobe levels. We present tables of the sidelobe levels and image fidelity. The most compact configurations provide the best brightness sensitivity, but suffer from antenna shadowing. Spiral configurations are more versatile and give better imaging fidelity for the source models considered.

1. Introduction

The CARMA telescope is being designed as a heterogeneous array with 10.4, 6.1 and 3.5 m antennas, and antenna configurations providing spacings from ~ 4 m to 2 km. Configurations with 5 radial arms are being considered for CARMA intermediate configurations (Mundy memo). These provide good uv coverage in ~ 4 hour observations with low sidelobes. The 5-armed star arrays were designed for 16 antennas. Six 10.4 and nine 6.1 m antennas will initially be used in the CARMA telescope. Changes to the largest antenna configuration are required to accommodate the boundaries and topography of the chosen site, and compact antenna configurations remain to be designed. The purpose of this memo is to compare the performance of various compact configurations.

We do not include the 3.5 m antennas in this analysis for a number of reasons. In the early years of CARMA, the 3.5 m antennas will be independently used for SZ observations using a separate correlator, and will not be available. The 3.5 m antennas will have receivers at λ 1 cm and 3 mm, but not 1 mm initially. The 6.1 m antennas will have receivers at λ 1 mm and 3 mm. Short spacings for λ 1 mm observations must be obtained from 6.1 and 10.4 m antennas. This does not preclude the use of 3.5 m antennas for specific observations, but we must design compact configurations to provide good imaging using only 6.1 and 10.4 m antennas, with an eye towards the future inclusion of additional antennas, including 3.5 m antennas.

In BIMA memo 84, we calculated the sensitivities for different sub-arrays of the CARMA antennas. Making all correlations of six 10.4, nine 6.1, and eight 3.5 m antennas requires 253 baselines per polarization. Most of the sensitivity, $\sim 90\%$ for both single field, and $\sim 80\%$ for mosaicing observations, can be obtained using a sub-array comprised of the 10.4 and 6.1 m antennas, requiring only 105 baselines per polarization. Additional correlator capacity can be used more effectively for increased bandwidth or dual polarization, than including the 3.5 m antennas. In section 7 we argue that pointing and primary beam errors will limit the image fidelity in mosaicing observations; this limits the usefulness of correlations between 10.4 and 3.5 m antennas in the heterogeneous array.

2. The fitting procedures

The fitting procedures are simple **unix csh** scripts which control **MIRIAD** tasks. The results from two scripts are presented here. These scripts are similar to those used for ALMA and ATA simulations, but are slightly more complex because of the different antenna sizes used in the heterogeneous CARMA telescope. The first script generates uv -data for a point source with thermal and atmospheric phase noise, does a phase calibration, and makes an image and beam. A Gaussian fit is made to the synthesised beam, and the results written into a table. The brightness sensitivity, beam FWHM, and residual sidelobe level after the fit are calculated. Timing information for each

¹This document is also BIMA Memo # 91

step is given. The script takes ~ 30 s run time for each instance on a Sparc 10 workstation and the procedure should be part of the observing preparation tools.

The second script makes model uv -data sampled by the heterogeneous array telescopes using a VLA image of Cas A as a model. The model is scaled to various source sizes and mosaic data are created for each pointing center and primary beam pattern. Thermal noise, appropriate for the CARMA telescopes is added to the uv -data. The uv -data is Fourier transformed to make images and deconvolved using Maximum Entropy (MEM) algorithms. The original image model is convolved to the same resolution by a Gaussian restoring beam and subtracted from the deconvolved image. The residual imaging errors are characterized by the total recovered flux, peak flux density and the RMS residuals. A control script invokes the imaging scripts for a selected range of source models, declinations and array configurations. A number of other parameters such as the uv -sample interval and mosaic pointing pattern were also varied to assess the behaviour of the simulated images.

The mosaicing process, the simulated images and the residual images are displayed on the terminal, and the images are saved on disk for further analysis. The numerical results are accumulated into a table. The script was run on a Sun ultra 10 with 250 kB of memory. Timing statistics were kept for each step. For 7-pointing mosaics with $\sim 30,000 - 60,000$ uv samples, each simulation takes $\sim 5 - 15$ min with most of the time taken by the MEM deconvolution. The procedure is simple enough and fast enough that an inexperienced user could explore the outcome of proposed or actual observations for a given source model and data sampling.

3. Data Sampling

For mosaic observations, a heterogeneous array can be considered as a set of sub-arrays for each primary beam pattern resulting from the cross correlations of 6.1×6.1 m, 10.4×10.4 m, and 6.1×10.4 m antennas. The primary beam pattern depends on the illumination of the antennas. In practice the mosaicing algorithms usually clip the primary beam response at the 5% level, thus avoiding the uncertainties and variations in the primary beam response at low levels. Within the 5% level, the primary beam pattern from the 6.1×10.4 m correlations is well approximated by a Gaussian beam pattern for an equivalent $\sqrt{10.4 \times 6.1} = 8.0$ m antenna.

Sampling rates are set by both the largest and smallest antenna diameter. The Nyquist sample interval for the uv data, $\delta uv = D/2\lambda$. The Nyquist sample interval for the pointings, $\delta\theta = \lambda/2D$. The number of pointings, $N_{pts} \sim \Omega/(\delta\theta)^2$. Thus the Nyquist sampling rate $\sim baseline/\lambda \times (2D_{max}/\lambda)^2 \times 2\lambda/D_{min} \times \Omega \times sdot$, where D is the antenna diameter, Ω , the source size, and $sdot = 2\pi/24/3600$). The uv data for each pointing are oversampled by the larger antennas, and the pointing is oversampled by the smaller antennas. There is no loss in sensitivity since the oversampled data are properly accounted for in the imaging algorithms. Using the larger antennas on the longest interferometer baselines provides a more uniform sensitivity in the uv data and reduces the required uv data sample rate.

4. Single Field Observations - star configurations.

The 5-arm radial star configurations provide scaled beams with resolutions from $\sim 0.2''$ in the a-array, $\sim 0.35''$ in the b-array and $\sim 0.9''$ in the c-array. Each array uses 5 stations from the next smallest array; requiring 35 stations for the three configurations. The positions of the antennas in the a-array depend on the boundaries and topology of each site. The Juniper site was used in this analysis. The site boundaries may be more restrictive and the resulting beams may have higher sidelobes in practice. The 15-antenna configurations are the same as the 16-antenna configurations, omitting the central antenna, which increases the peak sidelobes by less than $\sim 1\%$. Similar results are obtained by omitting other antennas. These configurations can be optimized to reduce the sidelobe levels, but any advantage is lost if an antenna is out of commission. The 5-arm radial star array pattern has the advantages of low infrastructure costs (shared stations, shorter fiber runs and roads) and lower environmental impact than more 2-dimensional configurations, but do require observations over a range of about 4 hours to provide good uv coverage.

Table 1 lists the beam FWHM, sensitivity, sidelobes levels, and fraction of the data remaining after shadowed data are omitted, for each configuration and source declinations from $+60$ to -40 deg. Each configuration was sampled from HA -2 to $+2$ hours, with an elevation limit of 10 degrees. We used natural weighting of the uv -data with a double sideband receiver temperature 80 K, an atmospheric model with zenith opacity 0.26 at 230 GHz, and a bandwidth 4 GHz. A zenith opacity 0.26 at 230 GHz corresponds to 4 mm of precipitable water at an altitude ~ 3000 m. With these parameters the single sideband system temperature ranged from 380 K at zenith to 2700 K at 10 degrees elevation.

In each configuration the 10.4 m antennas were positioned on the outer stations with two 10.4 m antennas on the northern arm. Assuming an aperture efficiency of 75%, we used antenna gains of 43, 126, and 73 Jy per K for the 10.4, 6.1, and cross correlations between 10.4 and 6.1 m antennas respectively. The weighting and sensitivities were calculated from the resulting system temperatures and antenna gains.

5. Compact Configurations

A merge of the 10-station BIMA d-array with the 5 inner stations of the star c-array provides a starting point for a compact configuration. Keeping the short spacings in the original BIMA d-array leaves rather a large gap to the 5 inner c-array stations. Optimization is possible at the cost of extra stations. Three optimizations were considered: Opt1) keep the 5 inner stations of the star c-array fixed, and optimize the uv coverage by moving the other 10 antennas. Opt2) keep 9 BIMA d-array antenna positions fixed and move the other 6 antennas. Opt3) optimize the uv coverage by moving all 15 antennas. Figure 2 shows the positions of the star c-array and BIMA d-array stations, and the optimized merged array, opt3-d.

The BIMA d-array suffers from antenna shadowing at low declinations. This has a large effect on the sensitivity of the heterogeneous 15-antenna array because when a 6.1 m antenna is shadowed, then all baselines to both 6.1 m and 10.4 m antennas are compromised. Shadowing is discussed in more detail in the next section.

Another difficulty with these ring+star configurations is the transition from the compact configuration to the higher resolution and much sparser uv coverage provided by the star c-array. Mosaicing simulations show that the star c-array has rather poor image fidelity due to the sparse uv coverage, making it difficult to enhance the resolution of the compact configuration.

This leads us to consider alternative compact array configurations. Logarithmic spiral configurations offer a central high density of uv samples with an approximately Gaussian uv distribution providing good beam sidelobes. Progressive increments in resolution are possible by positioning antennas at stations further out along a spiral pattern. The spiral configurations are more versatile and additional antennas can be easily incorporated.

Figure 3 shows three possible spiral configurations. The most compact, spiral5, has equal north-south and east-west geometry. The more extended, spiral6 and spiral7 configurations are stretched in the north-south direction by a factor 1.5 to give rounder beams at low declinations and alleviate shadowing.

Table 2 compares the synthesized beam FWHM, sidelobes and sensitivity for 5 compact configurations. The ring+star configurations have the largest synthesized beams and the best brightness sensitivity, but have poor uv coverage and reduced flux sensitivity at low declinations because of antenna shadowing. The spiral configurations have better uv coverage and flux sensitivity, but have smaller synthesized beams and consequently lower brightness sensitivity. Because of the logarithmic progression of antenna positions, the brightness sensitivity of the spiral configurations is more readily enhanced by convolution, especially if some 6.1 m antennas are positioned at larger radii. The stretched configuration, spiral6, gives constant beam areas and brightness sensitivity within 10% from declination +60 to -30 degrees.

6. Shadowing

Antenna shadowing depends on the height and relative placement of the 6.1 and 10.4 m antennas and cannot be calculated simply from the projected uv spacing. Shadowing and flagging of data is best done at the observatory from a model of the antenna structure and configuration.

In Table 3 we show the effect of flagging data using a 10.4 m diameter projected uv spacing instead of the 6.1 m diameter used in Table 2. The sensitivity and uv coverage are much better if the antennas are positioned so that a 6.1 m diameter represents the actual antenna shadowing situation at the observatory. This requires that the 6.1 m and 10.4 m antennas have larger separations than currently used in the BIMA d-array.

When an antenna is shadowed, all antenna pairs which include the shadowed antenna are omitted. Although the shortest baselines are excluded, this can also result in the loss of a large fraction of the uv coverage and collecting area of the array. The efficiency of the array can be improved by using configurations which are stretched in a north-south direction. The sensitivity and sidelobe levels are both improved.

Several possible effects of shadowing should be considered. i) a modified illumination pattern, ii) possible cross-talk between the shadowed antennas, iii) changes in the effective phase center of the antenna. We briefly discuss each of these.

i) A modified illumination pattern illumination pattern, gives a time and baseline dependent primary beam pattern. The change in the forward gain for a compact source is easily calculated, but the effective primary beam illumination for extended sources is more troublesome. For mosaic observations we would need to calculate a primary beam for each pointing, baseline, and integration. Whilst this is possible in principal, the increased computing burden is substantial, and the errors in the visibility data from pointing errors and uncertainties in the primary beam are large.

ii) Cross-talk between the shadowed antennas is not well understood. Sensitive experiments with closely spaced, and possibly shadowed antennas often corrupt the visibility data (e.g. Subrahmanyam 2002; Padin et al. 2001). Such cross-talk is not often seen at the BIMA array, where data are recorded for projected antenna spacings as short as half the antenna diameter. These data are flagged, but can be used at the discretion of the user. Apart from the loss in amplitude, no cross-talk is seen down to low levels. The reason for these differences are not clear.

iii) When an antenna is partially shadowed the projected spacing (u,v) is changed. In principal, this can be computed and recorded with the uv -data. If there are several closely packed antennas, this could be quite complicated, as different parts of the antenna structures shadow neighboring antenna surfaces. The phase center, defined by the intersection of the antenna axes is unchanged (at least to 1st order, ignoring the variations in the effective elevation axis for different parts of the antenna surface).

In view of these difficulties it seems better not to rely on the shadowed data, despite the appeal of shorter projected spacings and increased observing efficiency. One further effect which should be considered is the possibility of deleterious effects at zero fringe rate, when any cross talk is not distinguished from the source correlation. The fringe rate is $\dot{sdot} \times u \times \cos(\text{declination})$ Hz, where $\dot{sdot} = 7.25^{-5} s^{-1}$ and u is in wavelengths. Flagging these data over a Nyquist sample interval ~ 5 min leaves a $\sim 46\lambda/\cos(\text{declination})$ gap at $u = 0$. This is not a major gap in the uv -coverage for CARMA.

7. Primary Beams

The primary beam pattern illuminates the source brightness distribution, and is an important consideration for imaging sources which are large compared with the primary beam. The antenna focus, and subreflector position also affect the primary beam illumination. Primary beam and pointing errors dominate the image errors in a mosaic observation (Cornwell, Holdaway & Uson, 1993). Table 4 lists the primary beam FWHM at 230 GHz. The values listed are based on a Gaussian illumination. In practice the illumination is tapered to ~ -13 db at the edge of the dish, and the primary beam pattern is well fitted by a Gaussian with a FWHM about 6% larger. For a Gaussian illumination pattern, the primary beam radius at the 5% point is $1.04 \times$ the FWHM. Beyond the 5% point the beam pattern may have substantial variations with antenna elevation, subreflector position and temperature etc.

The primary beam model used in mosaic imaging algorithms must be truncated. This should occur at a radius where the primary beam correction is sufficiently small and before the errors become significant. Errors in the primary beam model can give substantial mosaic imaging errors. For a Gaussian illumination pattern truncated to -13 db at the edge of the dish, the effective primary beam between 10.4 and 6.1 m antennas is within about 1% of a Gaussian pattern corresponding to an 8 m antenna. The primary beam pattern for the 3.5 m antenna is not yet known; Table 4 lists the geometric mean for Gaussian patterns. The uncertainties in the primary beam pattern are greater than the errors made by treating the 10.4 to 6.1 m antenna beam as a Gaussian. For the 10.4 to 3.5 m correlations, large uncertainties in the 10.4 m voltage pattern lie well within the illumination pattern of the 3.5 m antennas. Similarly, if the pointing centers of the antennas are offset, there are large uncertainties in the resulting product of voltage patterns. Herein lies an opportunity and a challenge. If we can determine the primary beam patterns well enough, then including 10.4 versus 3.5 m correlations and offset pointings between all antennas provides additional information in the mosaicing process; the sky is multiplied by quite different primary beam patterns from the different combinations of antennas, in principle providing data to deconvolve the primary beam responses from the image. If we can not determine the primary beam patterns well enough, the errors will degrade the image fidelity. The current mosaicing algorithms can handle heterogeneous array imaging, but do not give realistic estimates of the image errors. A Chisq image gives some idea of the limiting noise. There is clearly a need for research in both determining the primary beam performance, and developing the mosaicing algorithms for heterogeneous array imaging.

In order to keep the number and parameterization of the primary beam models manageable, the most convenient way to make mosaicing observations is to use the same pointing pattern for all antennas at the sample interval required for the largest antenna in the sub-array being used. In view of the discussion above this mode is also likely to produce the best image fidelity in practice. Table 4 lists the Nyquist sample interval for each antenna. Larger areas of sky may be imaged using a larger sample interval at the cost of reduced image fidelity and variation of the noise level across the image (see BIMA memo 73).

8. Mosaicing Simulations

We made mosaicing simulations for three compact configurations of nine 6.1 and six 10.4 m antennas using a VLA image of Cas A as a model. The model was scaled to various source sizes and uv data created for each pointing center and primary beam pattern. Thermal noise, calculated using a double sideband receiver temperature 80 K, an atmospheric model with zenith opacity 0.26 at 230 GHz, with a bandwidth 4 GHz and the antenna gains for the CARMA telescopes, was added to the uv -data. The uv -data were Fourier transformed to make images and deconvolved using Maximum Entropy (MEM) algorithms. The original image model was convolved to the same resolution by a Gaussian restoring beam and subtracted from the deconvolved image. The residual imaging errors are characterized by the total recovered flux, peak flux density and the RMS residuals.

Mosaic images for source diameters $32''$, and $40''$ were modeled using a hexagonal pointing pattern with $15''$ spacing. A $32''$ diameter source lies within the primary beam of the 6.1 m antennas and mosaic observations with the 6.1 m antennas are not strictly required. The results for a $40''$ are listed in Table 5. The image fidelity is listed in the last column as the ratio of the peak flux density to the on-source RMS on the residual image. The RMS was evaluated in a standard bounding box $1.25 \times$ the image diameter.

Three different MEM deconvolutions were used: i) Using the interferometer data only with a total flux constraint. Single dish data were not included. ii) Using the single dish data as a default image. In this case, spatial frequencies obtained from the interferometer data deconvolution replace those from the single dish data. iii) Joint deconvolution of the interferometer and single dish data. In this case, the extent to which the single dish data can be deconvolved is limited by our characterization of the primary beam and pointing errors in the single dish data. These three deconvolutions are compared in Tables 5.1, 5.2 and 5.3. The thermal noise for each pointing was 1.4 mJy for the 6.1 m antennas, 0.76 mJy for the 10.4 m antennas, and 0.67 mJy for the cross correlations between 6.1 and 10.4 m antennas at dec +30. The corresponding numbers at dec -30 degrees are 3.5, 2.2, and 1.8 mJy per pointing.

The best image fidelity was obtained using the joint deconvolution of the interferometer and single dish data (Table 5.3). For the single dish data, we used the 10.4 m antennas, and set the noise level at 1% of the peak flux density, since we want the noise estimate for the single dish data to include primary beam and pointing errors. More than one 10.4 m antenna could be used to reduce random or systematic noise from pointing, primary beam and atmospheric fluctuations, but the data are treated here as one antenna with a 1% noise. Using the single dish data as a default image (Table 5.2), provides both a total flux estimate and low spatial frequencies unsampled by the interferometric mosaic. This gives higher image fidelity than just using the interferometer data with a total flux estimate (Table 5.1).

Giving higher weight to the single dish data, as in the joint deconvolution, improves the image fidelity, but may be unrealistic. In practice, primary beam and pointing errors will limit the image fidelity (Cornwell, Holdaway & Uson, 1993), but it is useful to compare the performance of the

three compact configurations without this limitation. The spiral configurations give better image fidelity than the star+ring configurations. The stretched spiral6 configuration is better at low declinations. The same result is obtained in all three deconvolution methods and is a result of the better uv sampling provided by the spiral configurations. The uv coverage for a ring+star and a spiral configuration for declinations +30, 0, and –30 degrees are shown in Figures 4 - 9.

A Maximum Entropy image using joint deconvolution and the residual image are shown in Figures 10 and 11 for a spiral configuration at declination +30 degrees. The error images for all the configurations and declinations considered show a residual bowl with edge brightness resulting from the defects in the deconvolution reconciling the constraints of the single dish data, the interferometer data and the bounding box for the deconvolution. These deconvolutions could be improved by tuning the parameters (noise level estimates, bounding box, etc), but we wish to compare the different compact configurations in a uniform way. In practice, the imaging errors will be dominated by noise and systematic errors in the uv data and deconvolution errors at these levels will not be significant for most sources.

9. Conclusions

Three radial star configurations provide scaled beams with resolutions from $\sim 0.15''$ to $\sim 0.9''$ at 230 GHz. Each array uses 5 stations from the next smallest array, requiring 35 stations for the three configurations. Star configurations have low infrastructure costs (shared stations, shorter fiber runs and roads), but provide a sparse uv sampling for imaging extended sources. For mosaicing we need to sample the uv for each pointing center, and more 2-dimensional configurations are desirable for the compact configurations which are needed for larger source sizes.

We consider ring and spiral compact configurations. The ring arrays give the best brightness sensitivity and require the fewest stations, but suffer from antenna shadowing. Another difficulty with the ring+star configurations is the transition from the compact configuration to the higher resolution and much sparser uv coverage provided by the star configuration, making it difficult to enhance the resolution of the compact configuration. Logarithmic spiral configurations have a central high density of uv samples with an approximately Gaussian uv distribution providing good beam side-lobes. Progressive increments in resolution are possible by positioning antennas at stations further out along a spiral pattern. The spiral configurations are more versatile and additional antennas can be easily incorporated at the cost of additional antenna stations. Mosaicing simulations show that the spiral configurations give better image fidelity than the star+ring configurations. The best image fidelity was obtained using a joint deconvolution of the interferometer and single dish data from 10.4 m antennas. A joint deconvolution gives higher weight to the single dish data than using the single dish data as a default image or to provide a total flux estimate. In practice, pointing and primary beam errors will limit the image fidelity, and the single dish data may have significant errors. Short spacings from a 3.5 m antenna compact subarray could be used to complement the 6.1 and 10.4 m baselines when the 3.5 m antennas become available at λ mm wavelengths.

10. References

- "Image Fidelity", M.C.H. Wright, 1999, BIMA memo 73, <http://bima.astro.umd.edu/memo/memo.html>
- "An approach to interferometric mosaicing", Sault, R.J., Staveley-Smith, L & Brouw, W.N., 1996, A&A Supp., 120, 375
- "Miriad Users Guide", 1999, Bob Sault & Neil Killeen, <http://www.atnf.csiro.au/computing/software/miriad>
- "Mosaicing with Interferometer Arrays", Holdaway. M.A., 1999, ASP Conference series 180, 401.
- "Radio-interferometric imaging of very large objects: implications for array design", Cornwell, T.J., Holdaway, M.A. & Uson, J.M., 1993, A&A 271, 697.
- "Cross-talk in Close-packed Interferometer Arrays", Ravi Subrahmanyan, 2002, ATCA memo.

Table 1: Radial Configurations

Config	DEC	RMS[mJy]	Beam [arcsec]	Tb rms[mK]	Sidelobe[%]: RMS	Max	Min	Nvis[%]
ja-1	60	0.24	0.17 x 0.16	204.0	1.5	6.5	-7.7	100
ja-1	45	0.23	0.16 x 0.15	221.6	1.6	7.4	-8.0	100
ja-1	30	0.23	0.16 x 0.15	221.6	1.7	9.9	-8.1	100
ja-1	15	0.24	0.17 x 0.16	204.0	2.0	13.0	-8.1	100
ja-1	0	0.27	0.20 x 0.16	195.1	2.6	28.8	-8.2	100
ja-1	-15	0.34	0.26 x 0.16	189.0	1.9	11.9	-7.9	100
ja-1	-30	0.57	0.38 x 0.17	204.0	1.5	8.4	-8.0	100
ja-1	-40	1.37	0.62 x 0.17	300.5	1.4	8.5	-7.7	100
jb-1	60	0.24	0.34 x 0.31	52.6	1.8	11.2	-6.2	100
jb-1	45	0.23	0.34 x 0.29	53.9	1.9	10.3	-6.1	100
jb-1	30	0.23	0.34 x 0.29	53.9	1.9	11.7	-6.3	100
jb-1	15	0.24	0.34 x 0.31	52.6	2.1	18.4	-6.8	100
jb-1	0	0.27	0.36 x 0.34	51.0	2.5	35.4	-8.0	100
jb-1	-15	0.34	0.47 x 0.34	49.2	2.0	12.5	-6.4	100
jb-1	-30	0.57	0.72 x 0.35	52.3	1.7	11.6	-6.3	100
jb-1	-40	1.37	1.17 x 0.36	75.2	1.5	10.9	-7.9	100
jc-1	60	0.24	0.84 x 0.77	8.6	1.8	11.2	-6.2	100
jc-1	45	0.23	0.85 x 0.72	8.7	1.9	10.3	-6.1	100
jc-1	30	0.23	0.85 x 0.72	8.7	1.9	11.7	-6.3	100
jc-1	15	0.24	0.85 x 0.77	8.5	2.1	18.4	-6.8	100
jc-1	0	0.27	0.90 x 0.84	8.3	2.5	35.4	-8.0	100
jc-1	-15	0.34	1.17 x 0.86	7.8	2.0	12.4	-6.4	100
jc-1	-30	0.57	1.81 x 0.88	8.3	1.7	11.6	-6.3	100
jc-1	-40	1.37	2.92 x 0.90	12.1	1.5	10.9	-7.9	100

Table 2: Compact Configurations

Config	DEC	RMS[mJy]	Beam [arcsec]	Tb rms[mK]	Sidelobe[%]: RMS	Max	Min	Nvis[%]
opt1-d	60	0.24	4.22 x 3.82	0.3	1.8	9.8	-7.0	100
opt1-d	45	0.23	3.98 x 3.82	0.3	2.0	10.5	-7.0	100
opt1-d	30	0.23	4.00 x 3.83	0.3	2.2	11.5	-7.0	100
opt1-d	15	0.24	4.29 x 3.83	0.3	2.4	13.0	-7.1	100
opt1-d	0	0.28	4.96 x 3.80	0.3	2.8	36.7	-12.0	97
opt1-d	-15	0.36	6.04 x 3.72	0.4	2.3	15.1	-7.4	87
opt1-d	-30	0.71	7.97 x 3.39	0.6	2.4	14.4	-9.6	54
opt1-d	-40	1.97	11.03 x 3.09	1.3	2.2	16.6	-12.3	37
opt2-d	60	0.24	4.80 x 4.25	0.3	1.7	11.7	-6.8	100
opt2-d	45	0.23	4.52 x 4.23	0.3	1.8	13.1	-6.9	100
opt2-d	30	0.23	4.53 x 4.23	0.3	1.9	13.2	-7.0	100
opt2-d	15	0.24	4.86 x 4.25	0.3	2.2	16.5	-7.0	100
opt2-d	0	0.27	5.64 x 4.24	0.3	2.9	35.1	-11.5	98
opt2-d	-15	0.35	7.35 x 4.24	0.3	2.2	17.7	-7.2	93
opt2-d	-30	0.68	10.73 x 3.96	0.4	2.2	14.8	-9.2	62
opt2-d	-40	2.46	18.32 x 3.59	0.9	2.6	22.6	-17.8	25
opt3-d	60	0.24	4.72 x 4.21	0.3	1.6	11.2	-6.6	99
opt3-d	45	0.23	4.44 x 4.14	0.3	1.7	11.3	-6.9	96
opt3-d	30	0.24	4.42 x 4.10	0.3	1.9	10.8	-7.1	92
opt3-d	15	0.25	4.68 x 4.12	0.3	2.1	11.6	-6.8	90
opt3-d	0	0.28	5.37 x 4.13	0.3	2.7	29.7	-11.7	86
opt3-d	-15	0.36	6.89 x 4.10	0.3	2.2	11.3	-7.1	81
opt3-d	-30	0.71	10.05 x 3.84	0.4	2.2	12.2	-9.1	55
opt3-d	-40	2.40	16.26 x 3.39	1.0	2.6	26.8	-16.6	24
spiral5	60	0.24	2.99 x 2.87	0.6	1.7	6.6	-6.3	100
spiral5	45	0.23	2.86 x 2.80	0.7	1.8	7.2	-7.4	100
spiral5	30	0.23	2.86 x 2.81	0.7	1.9	8.4	-6.7	100
spiral5	15	0.24	3.02 x 2.87	0.6	2.2	11.3	-6.7	100
spiral5	0	0.27	3.51 x 2.88	0.6	2.9	39.4	-12.4	100
spiral5	-15	0.35	4.38 x 2.81	0.7	2.4	10.7	-7.5	90
spiral5	-30	0.61	6.36 x 2.80	0.8	1.9	11.5	-7.3	76
spiral5	-40	1.67	9.24 x 2.50	1.7	2.1	17.8	-9.7	48
spiral6	60	0.24	2.82 x 2.03	1.0	1.7	7.3	-6.5	100
spiral6	45	0.23	2.82 x 1.89	1.0	1.9	7.9	-6.6	100
spiral6	30	0.23	2.83 x 1.89	1.0	2.1	13.6	-7.9	100
spiral6	15	0.24	2.84 x 2.03	1.0	2.4	17.1	-6.8	100
spiral6	0	0.27	2.85 x 2.35	0.9	2.6	35.7	-7.8	100
spiral6	-15	0.34	3.04 x 2.87	0.9	2.0	15.4	-6.6	100
spiral6	-30	0.59	4.52 x 2.81	1.1	1.9	8.5	-6.6	88
spiral6	-40	1.53	7.09 x 2.70	1.8	1.9	10.8	-7.1	70

Table 3: Effect of 10.4 m shadow on Compact Configurations

Config	DEC	RMS[mJy]	Beam [arcsec]	Tb rms[mK]	Sidelobe[%]: RMS	Max	Min	Nvis[%]
opt3-d	30	0.29	3.82 x 3.43	0.5	2.6	16.9	-10.1	43
opt3-d	0	0.42	4.20 x 3.33	0.7	4.1	44.6	-14.0	29
opt3-d	-30	1.59	12.41 x 2.53	1.2	6.4	37.1	-29.6	6
spiral5	30	0.26	2.43 x 2.38	1.0	2.3	15.1	-8.3	63
spiral5	0	0.31	2.96 x 2.44	1.0	3.5	34.8	-16.9	62
spiral5	-30	0.74	4.98 x 2.07	1.7	2.5	18.7	-12.1	31
spiral6	30	0.24	2.71 x 1.80	1.1	2.2	12.5	-7.3	87
spiral6	0	0.30	2.57 x 2.13	1.3	3.0	36.6	-8.6	75
spiral6	-30	0.69	3.83 x 2.26	1.8	2.4	10.7	-9.3	45

Table 4: Primary Beam at 230 GHz

Antennas	Equivalent diameter	FWHM	Nyquist interval
m x m	m	arcsec	arcsec
10.4 x 10.4	10.4	28	12.5
10.4 x 6.1	8.0	36	
6.1 x 6.1	6.1	47	21.3
10.4 x 3.5	6.0	48	
6.1 x 3.5	4.6	63	
3.5 x 3.5	3.5	83	37.1

Table 5.1: Mosaicing Simulations for Compact Configurations - total flux constraint

Config	DEC	Beam[arcsec]	Model Flux	Peak	Image Flux	Peak	Rms	Max	Min[Jy]	Fidelity
opt3-d	30	4.23 x 3.75	731.47	24.23	791.36	23.93	0.36	1.01	-0.76	66
opt3-d	15	4.47 x 3.81	731.46	25.59	788.77	25.37	0.32	0.94	-0.71	79
opt3-d	0	5.14 x 3.87	731.42	28.84	787.74	29.07	0.32	0.91	-0.81	92
opt3-d	-15	6.63 x 3.90	731.25	35.22	790.29	35.51	0.46	1.28	-1.08	78
opt3-d	-30	9.46 x 3.59	730.57	42.55	797.63	42.45	0.76	2.20	-1.75	56
spiral5	30	2.86 x 2.80	731.58	14.29	796.19	14.30	0.10	0.33	-0.39	139
spiral5	15	3.01 x 2.86	731.58	15.11	790.01	15.15	0.11	0.40	-0.31	143
spiral5	0	3.54 x 2.86	731.57	17.10	774.47	17.14	0.11	0.38	-0.29	162
spiral5	-15	4.71 x 2.90	731.53	21.45	772.30	21.45	0.14	0.46	-0.35	155
spiral5	-30	6.80 x 2.93	731.31	28.30	775.00	28.17	0.26	0.84	-0.55	109
spiral6	30	2.93 x 1.87	731.58	10.57	818.85	10.57	0.14	0.46	-0.28	78
spiral6	15	2.91 x 2.01	731.58	11.15	812.42	11.23	0.10	0.39	-0.25	109
spiral6	0	2.87 x 2.33	731.58	12.41	819.73	12.54	0.12	0.44	-0.38	106
spiral6	-15	3.03 x 2.86	731.58	15.19	785.73	15.16	0.10	0.35	-0.29	152
spiral6	-30	4.91 x 2.92	731.52	22.24	793.10	22.37	0.19	0.64	-0.45	120

Table 5.2: Mosaicing Simulations for Compact Configurations - default image constraint

Config	DEC	Beam[arcsec]	Model Flux	Peak	Image Flux	Peak	Rms	Max	Min[Jy]	Fidelity
opt3-d	30	4.23 x 3.75	731.47	24.23	783.85	23.96	0.32	0.96	-0.67	74
opt3-d	15	4.47 x 3.81	731.46	25.59	781.71	25.38	0.29	0.91	-0.62	86
opt3-d	0	5.14 x 3.87	731.42	28.84	780.24	29.00	0.29	0.89	-0.73	99
opt3-d	-15	6.63 x 3.90	731.25	35.22	781.98	35.42	0.42	1.21	-0.96	84
opt3-d	-30	9.46 x 3.59	730.57	42.55	784.63	42.24	0.69	2.09	-1.52	61
spiral5	30	2.86 x 2.80	731.58	14.29	784.25	14.26	0.09	0.28	-0.33	160
spiral5	15	3.01 x 2.86	731.58	15.11	779.62	15.13	0.09	0.32	-0.26	164
spiral5	0	3.54 x 2.86	731.57	17.10	768.77	17.14	0.10	0.37	-0.29	175
spiral5	-15	4.71 x 2.90	731.53	21.45	766.45	21.44	0.13	0.44	-0.31	168
spiral5	-30	6.80 x 2.93	731.31	28.30	767.86	28.13	0.24	0.84	-0.50	117
spiral6	30	2.93 x 1.87	731.58	10.57	789.88	10.58	0.10	0.32	-0.26	105
spiral6	15	2.91 x 2.01	731.58	11.15	788.81	11.20	0.08	0.28	-0.23	135
spiral6	0	2.87 x 2.33	731.58	12.41	791.88	12.49	0.09	0.36	-0.35	133
spiral6	-15	3.03 x 2.86	731.58	15.19	774.02	15.14	0.09	0.33	-0.26	172
spiral6	-30	4.91 x 2.92	731.52	22.24	777.96	22.32	0.16	0.56	-0.35	138

Table 5.3: Mosaicing Simulations for Compact Configurations - joint deconvolution

Config	DEC	Beam[arcsec]	Model Flux	Peak	Image Flux	Peak	Rms	Max	Min[Jy]	Fidelity
opt3-d	30	4.23 x 3.75	731.47	24.23	734.82	23.83	0.10	0.42	-0.38	229
opt3-d	15	4.47 x 3.81	731.46	25.59	734.87	25.12	0.12	0.46	-0.36	213
opt3-d	0	5.14 x 3.87	731.42	28.84	734.99	28.51	0.15	0.57	-0.36	185
opt3-d	-15	6.63 x 3.90	731.25	35.22	735.92	34.76	0.26	0.90	-0.53	135
opt3-d	-30	9.46 x 3.59	730.57	42.55	736.53	41.42	0.49	1.65	-0.88	84
spiral5	30	2.86 x 2.80	731.58	14.29	734.49	14.07	0.04	0.18	-0.15	380
spiral5	15	3.01 x 2.86	731.58	15.11	734.54	14.96	0.04	0.20	-0.18	356
spiral5	0	3.54 x 2.86	731.57	17.10	742.17	17.16	0.15	0.60	-0.37	117
spiral5	-15	4.71 x 2.90	731.53	21.45	734.36	21.24	0.08	0.37	-0.31	256
spiral5	-30	6.80 x 2.93	731.31	28.30	735.24	27.78	0.18	0.71	-0.41	154
spiral6	30	2.93 x 1.87	731.58	10.57	745.11	10.42	0.13	0.36	-0.32	82
spiral6	15	2.91 x 2.01	731.58	11.15	735.40	11.05	0.03	0.17	-0.13	409
spiral6	0	2.87 x 2.33	731.58	12.41	734.25	12.29	0.04	0.17	-0.17	351
spiral6	-15	3.03 x 2.86	731.58	15.19	733.71	14.98	0.04	0.18	-0.16	365
spiral6	-30	4.91 x 2.92	731.52	22.24	734.59	22.06	0.09	0.38	-0.21	248

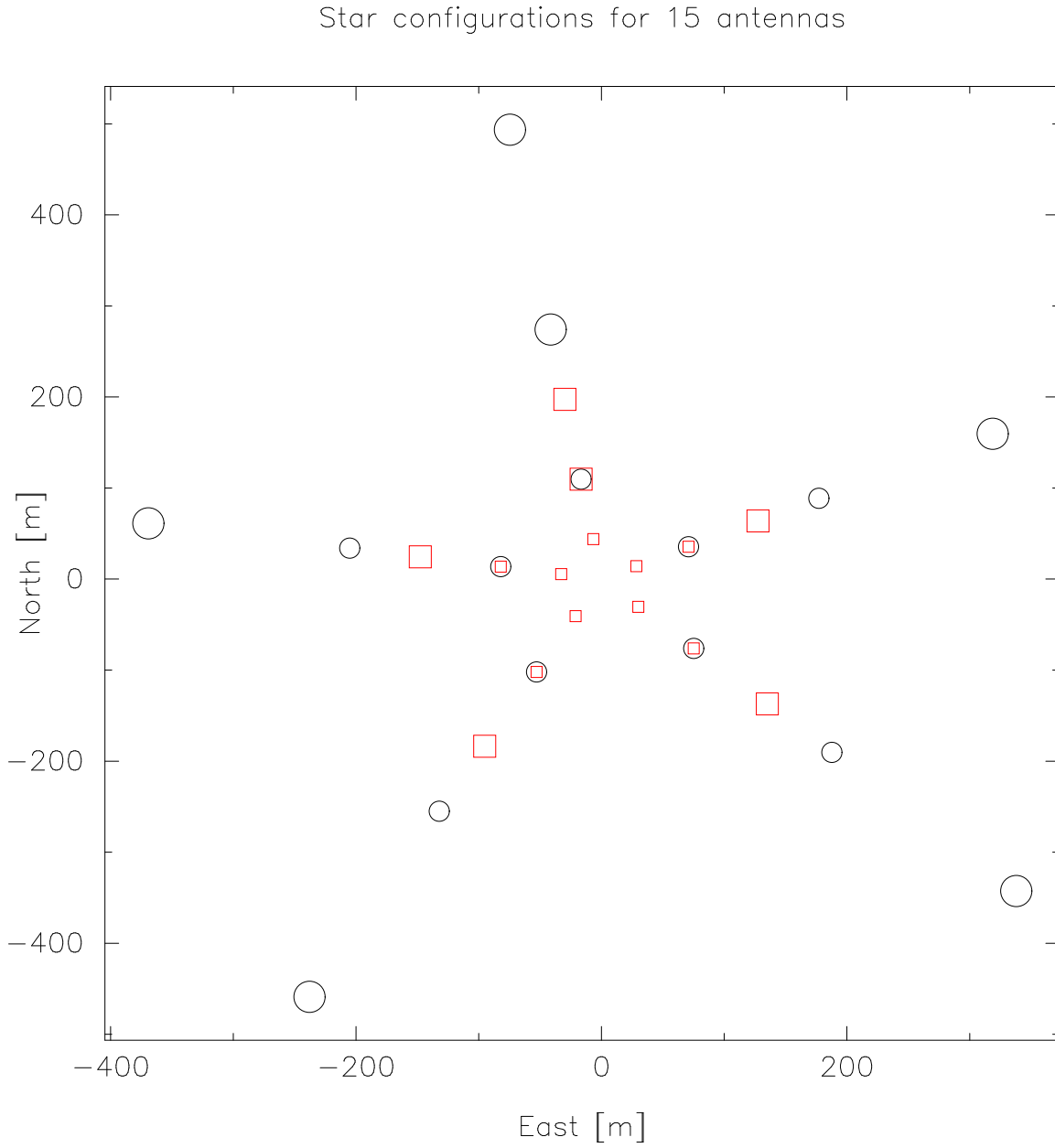


Fig. 1.— Star configurations. Black circles for b-array and red squares for c-array. The larger symbols show the positions of the 10.4 m antennas.

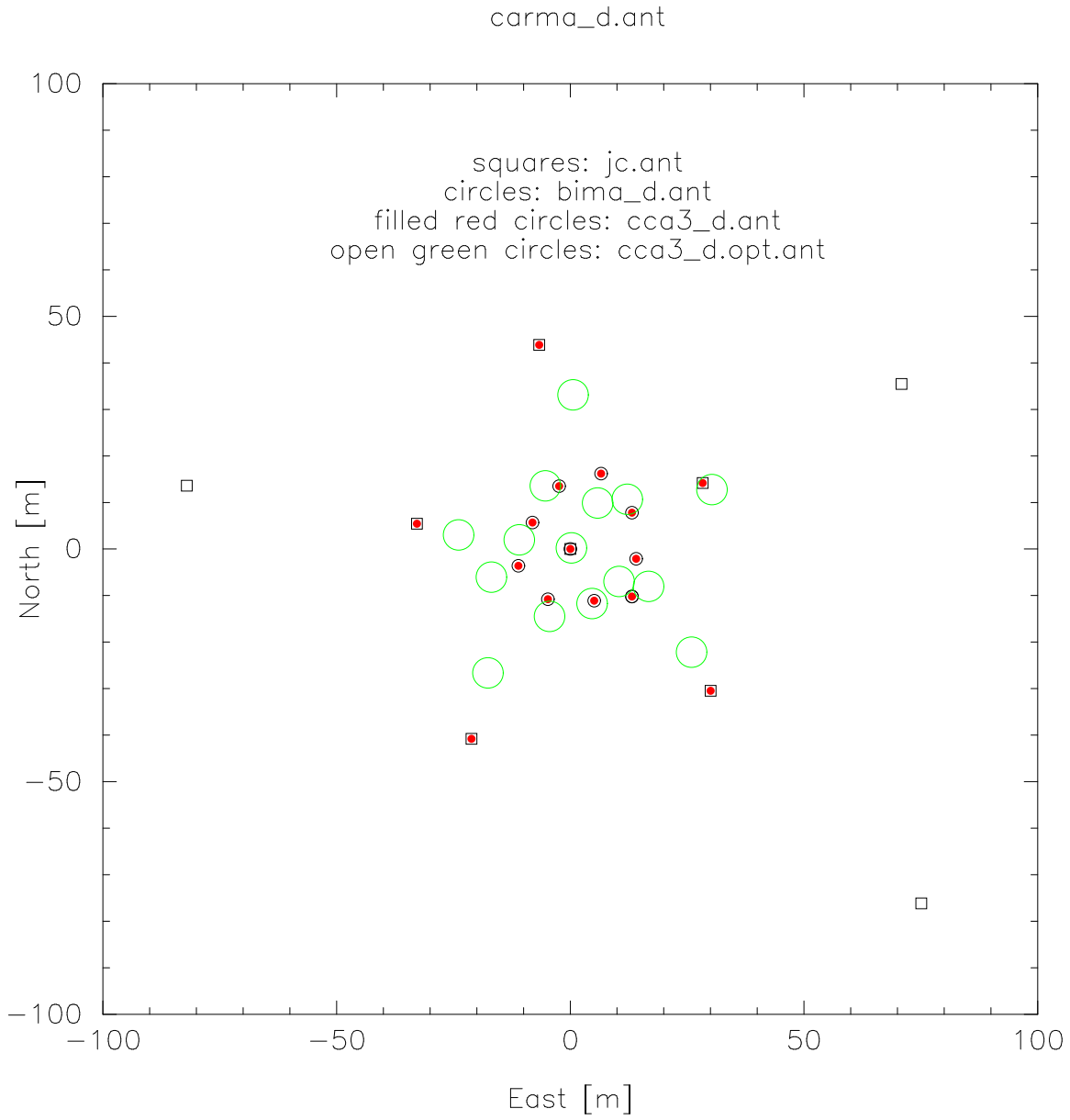


Fig. 2.— merged star array and BIMA d-array

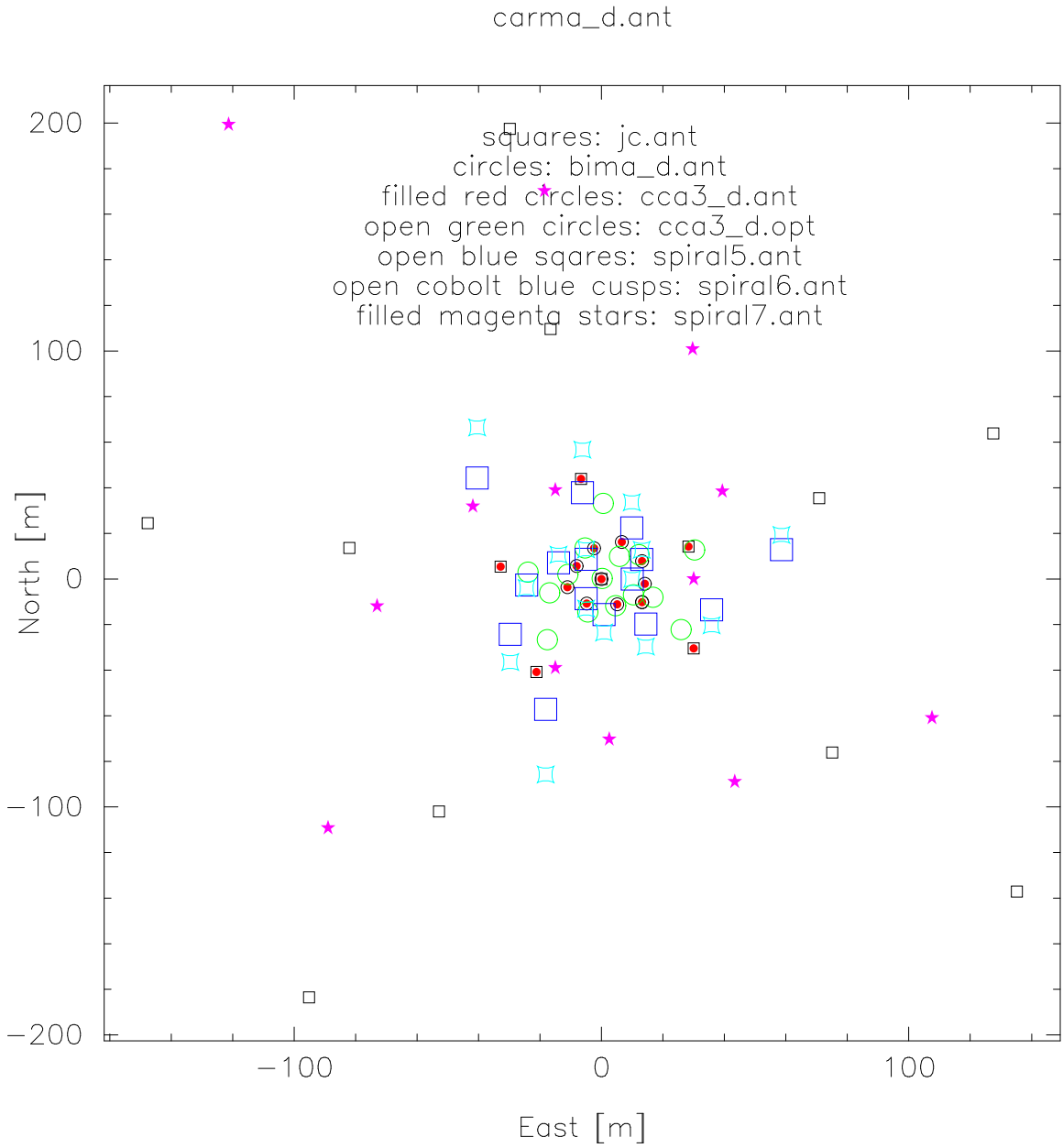


Fig. 3.— spiral array configurations

I 230.0000 GHz

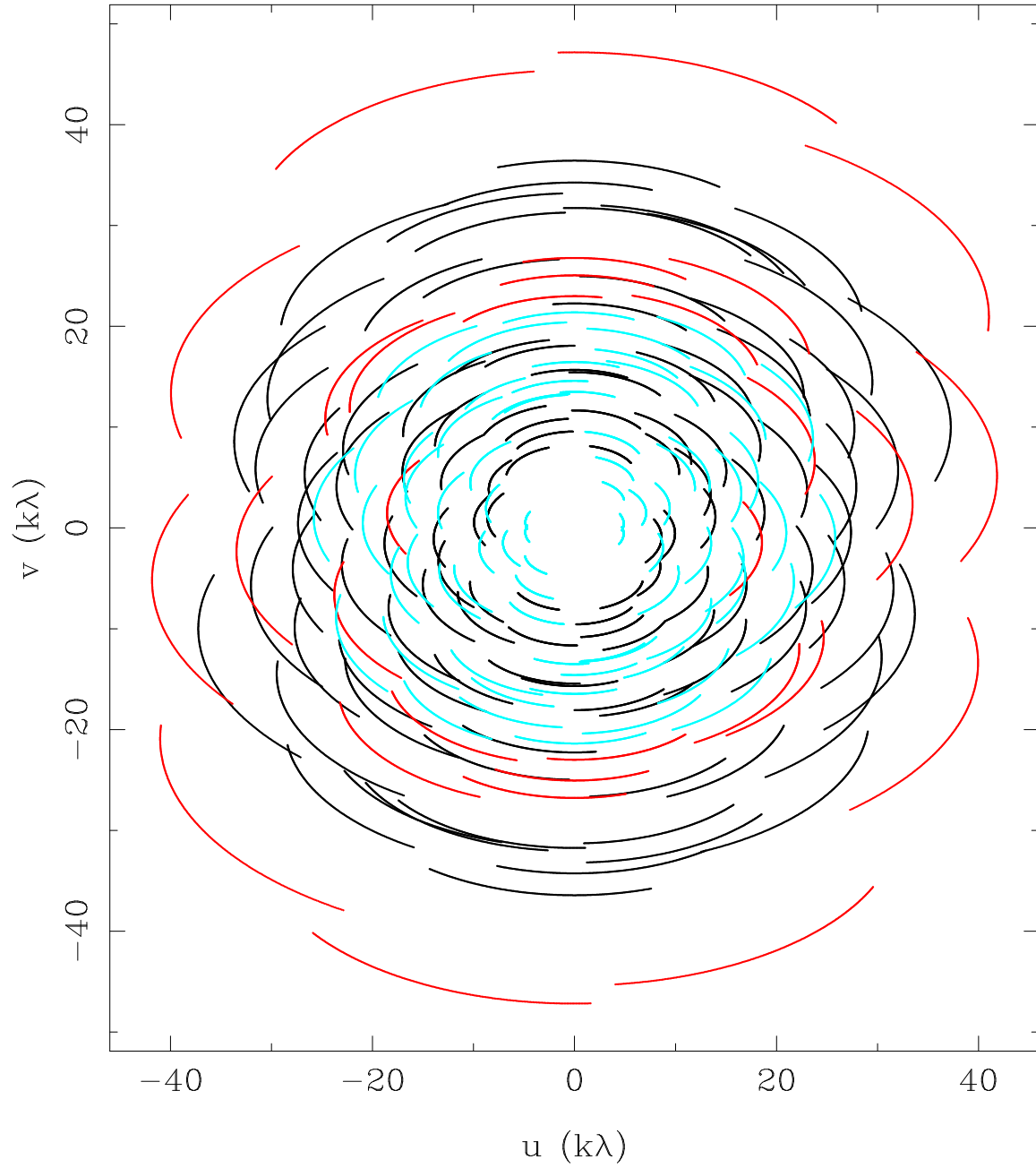


Fig. 4.— uv coverage for merged star array and BIMA d-array, opt3-d at declination +30 deg. 10.4 m x 10.4 m correlations in red, 6.1 m x 6.1 m in blue, and 6.1 m x 10.4 m in black.

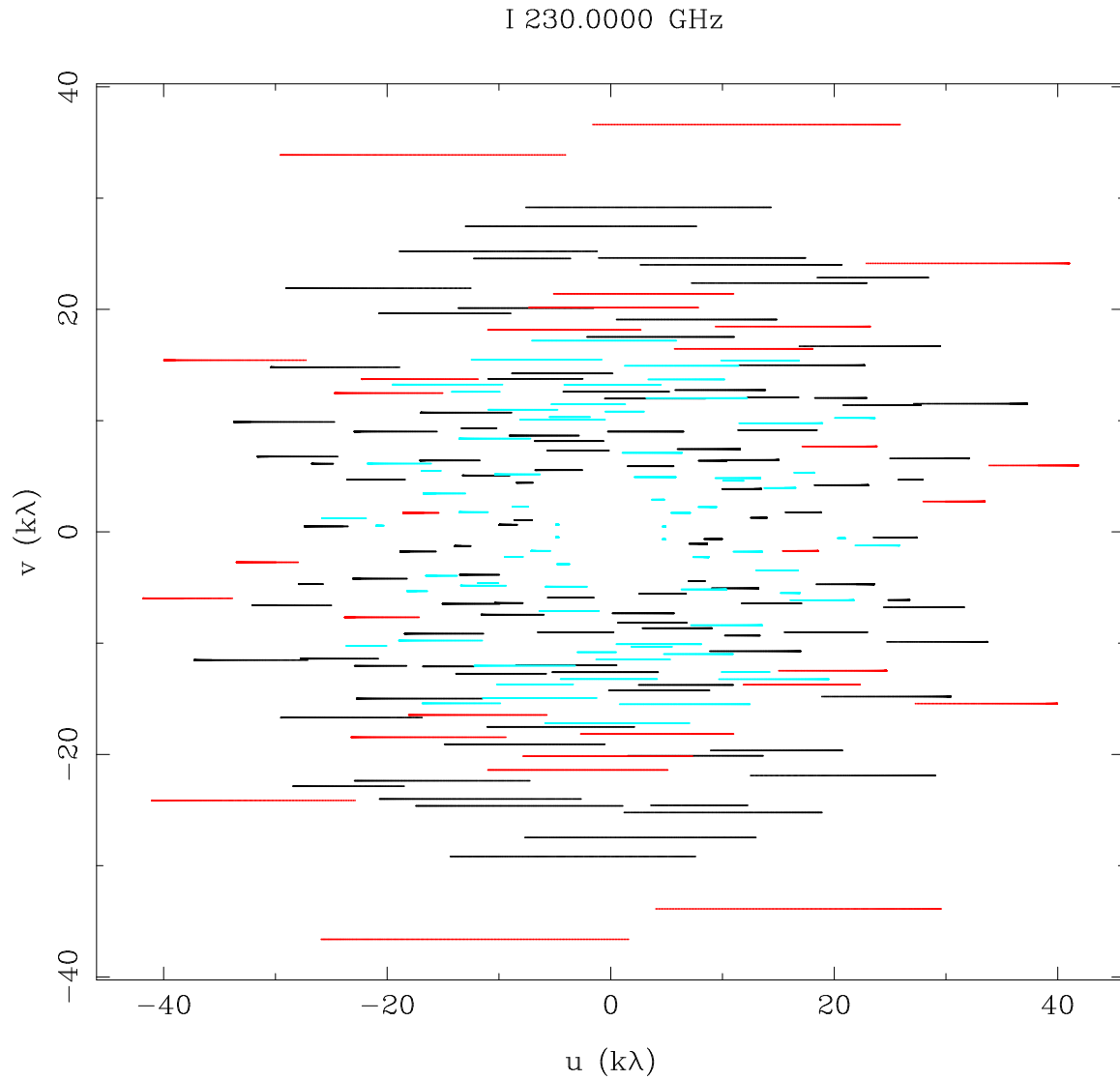


Fig. 5.— uv coverage for merged star array and BIMA d-array, opt3-d at declination 0 deg. 10.4 m x 10.4 m correlations in red, 6.1 m x 6.1 m in blue, and 6.1 m x 10.4 m in black.

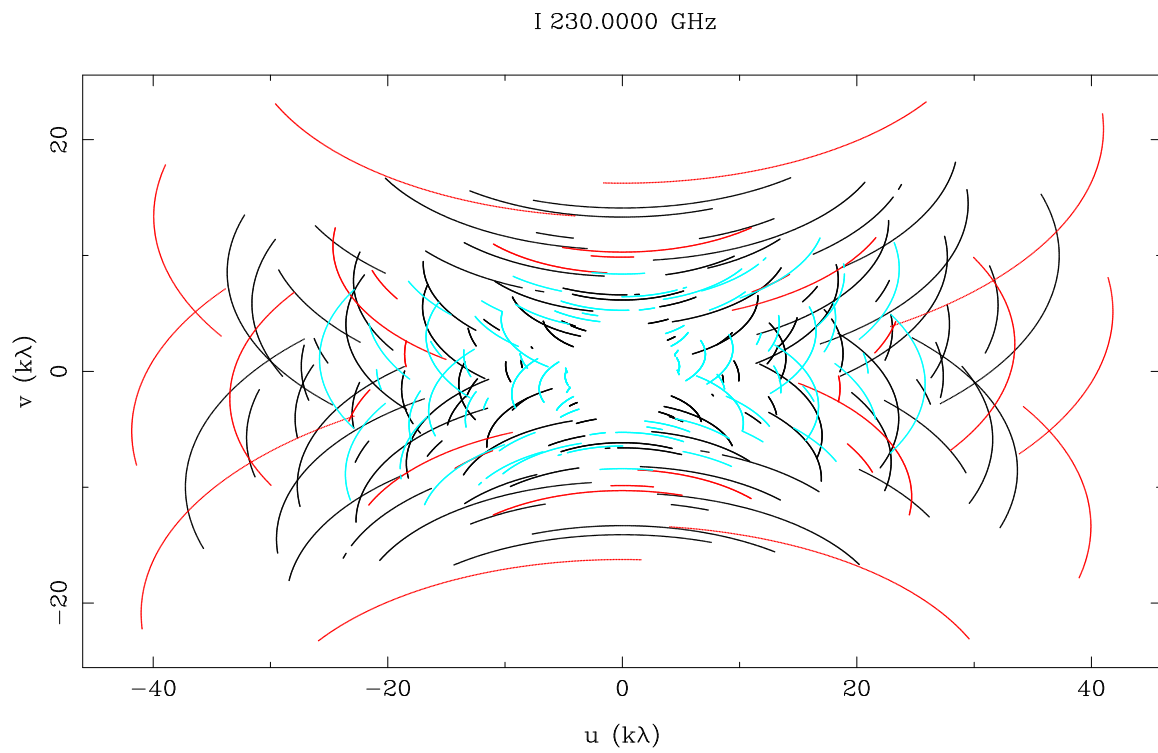


Fig. 6.— uv coverage for merged star array and BIMA d-array, opt3-d at declination -30 deg. 10.4 m \times 10.4 m correlations in red, 6.1 m \times 6.1 m in blue, and 6.1 m \times 10.4 m in black.

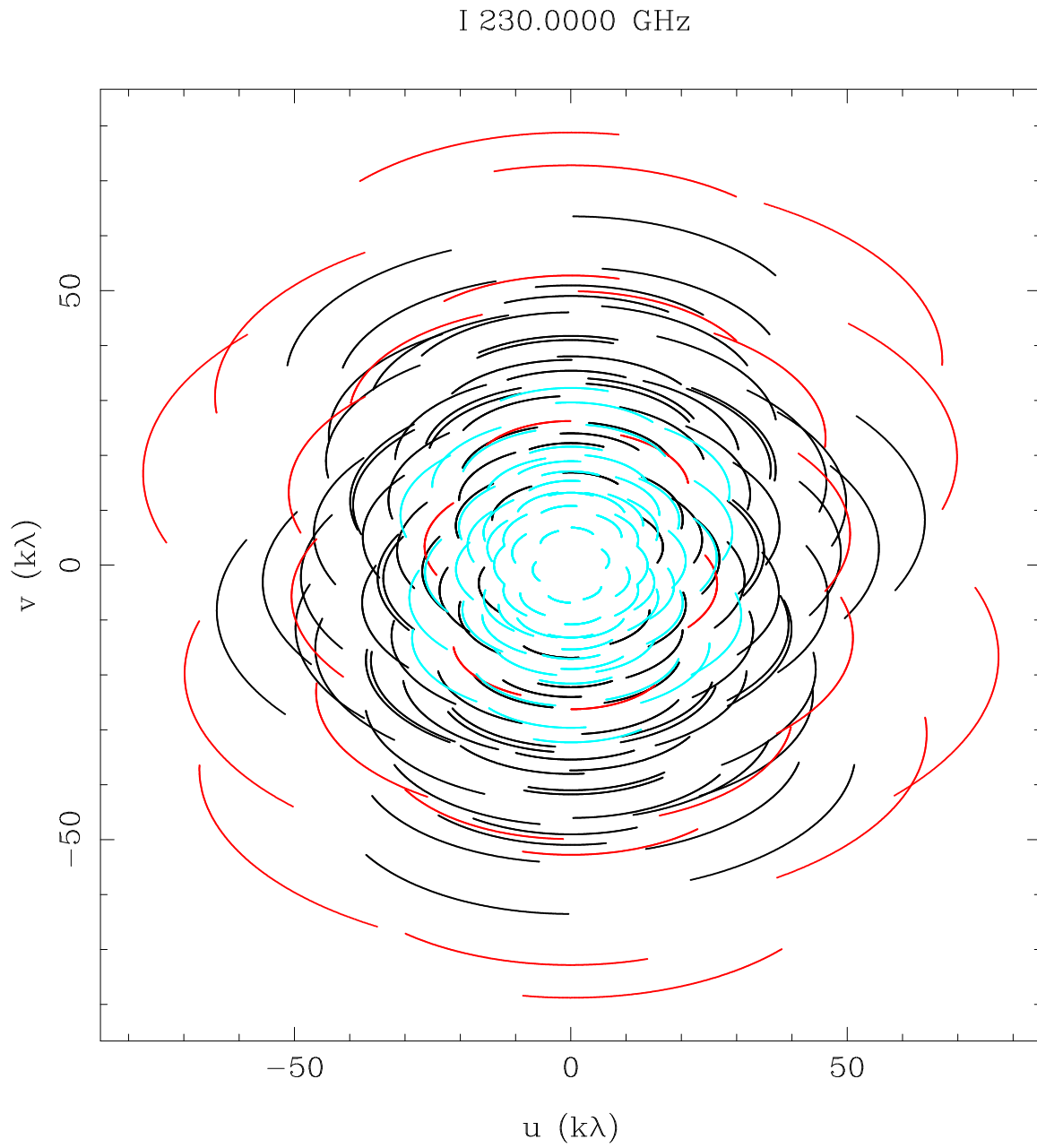


Fig. 7.— uv coverage for spiral configuration, spiral5, at declination +30 deg. 10.4 m x 10.4 m correlations in red, 6.1 m x 6.1 m in blue, and 6.1 m x 10.4 m in black.

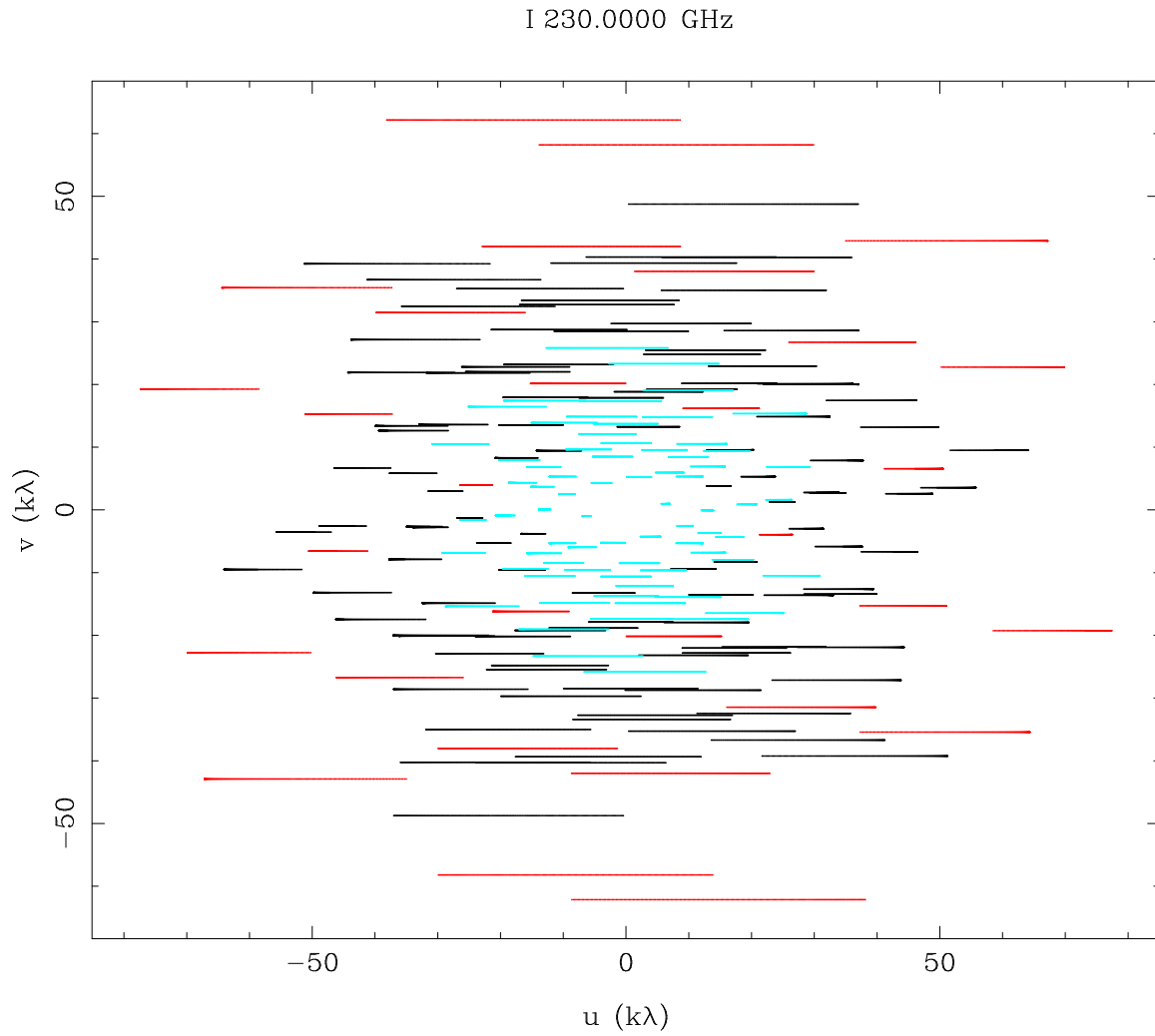


Fig. 8.— uv coverage for spiral configuration, spiral5, at declination 0 deg. 10.4 m x 10.4 m correlations in red, 6.1 m x 6.1 m in blue, and 6.1 m x 10.4 m in black.

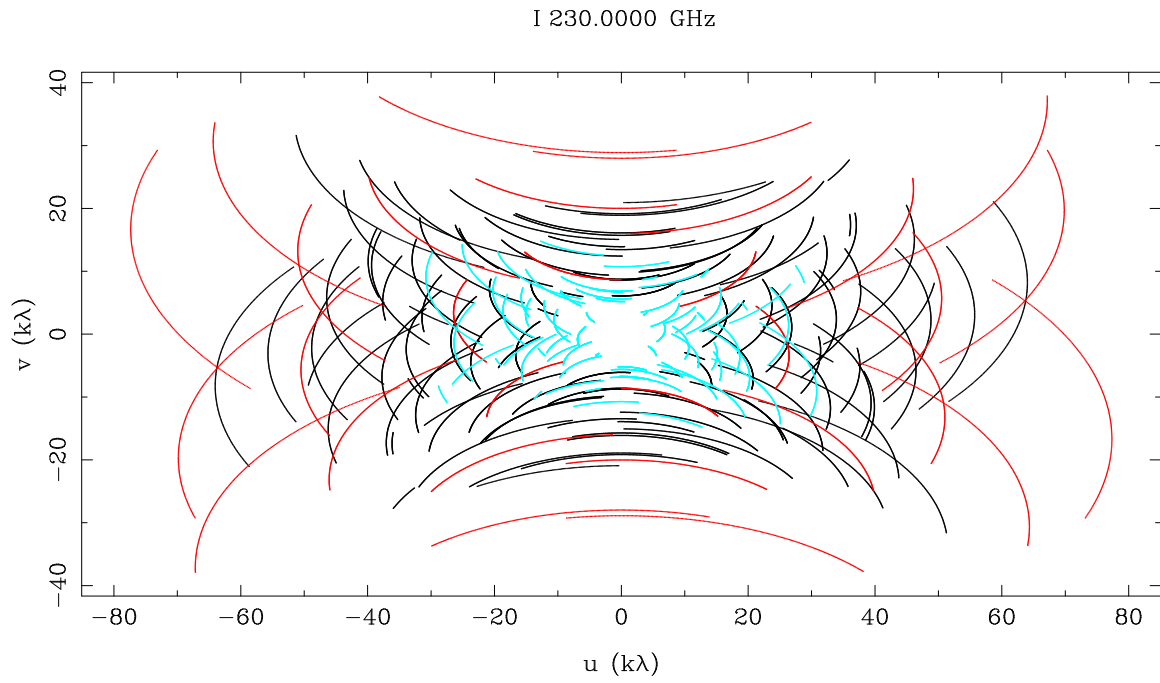


Fig. 9.— uv coverage for spiral configuration, spiral5, at declination -30 deg. 10.4 m \times 10.4 m correlations in red, 6.1 m \times 6.1 m in blue, and 6.1 m \times 10.4 m in black.

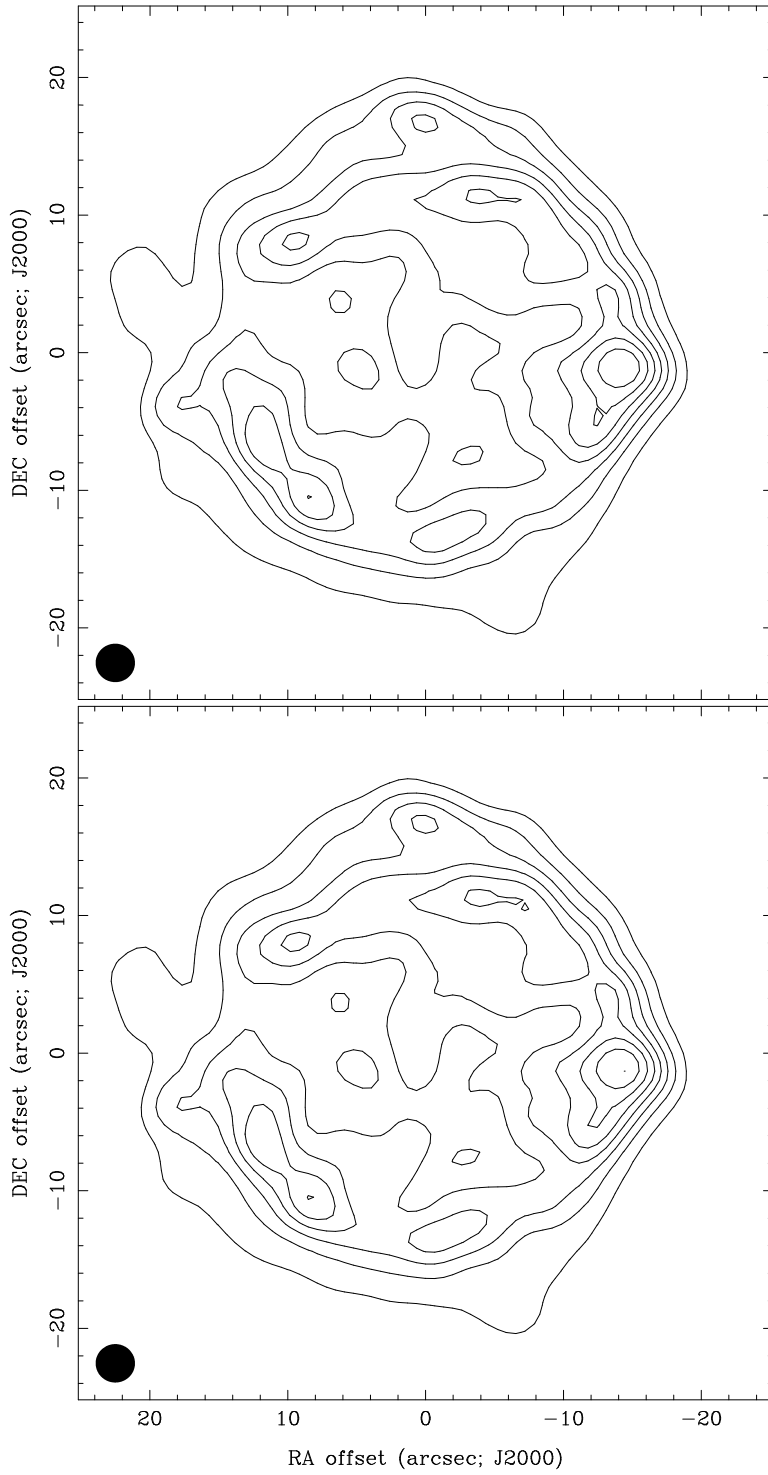


Fig. 10.— Maximum Entropy Image [upper panel] and Cas A model [lower panel] scaled to $32''$ diameter, imaged with CARMA compact configuration (spiral5) at declination $+30$ deg. Contours at 12.5%.

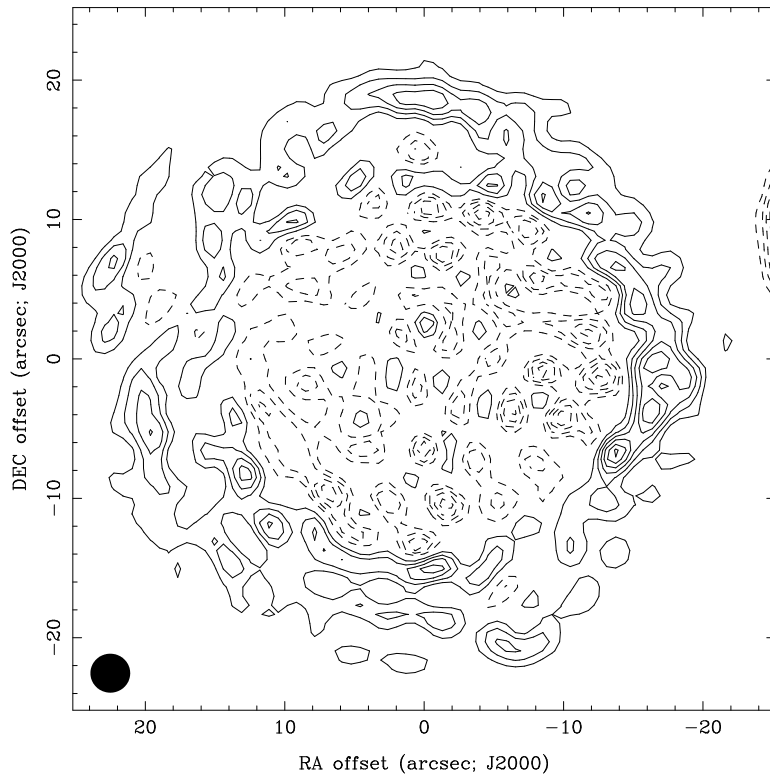


Fig. 11.— Residual Image for spiral5 configuration at declination +30 deg. using joint deconvolution of heterogeneous array and 10.4 m single dish data. Contours at 0.2% of Maximum Entropy Image.